

## Least-squares RTM: Reality and possibilities for subsalt imaging

Ping Wang\*, Adriano Gomes, Zhigang Zhang, and Ming Wang, CGG

### Summary

We investigated how current least-squares reverse time migration (LSRTM) methods perform on subsalt images. First, we compared the formulation of data-domain vs. image-domain least-squares migration (LSM), as well as methods using single-iteration approximation vs. iterative inversion. Next, we examined the resulting subsalt images of several LSRTM methods applied on both synthetic and field data. Among our tests, we found image-domain single-iteration LSRTM methods, including an extension from Guitton's (2004) method in the curvelet domain, not only compensated for amplitude loss due to poor illumination caused by complex salt bodies, but also produced subsalt images with fewer migration artifacts in the field data. By contrast, an iterative inversion method showed its potential for broadening bandwidth in the subsalt, but was less effective in reducing noise. Based on our understanding, we summarize the current state of LSRTM for subsalt imaging, especially between single-iteration and iterative LSRTM methods.

### Introduction

We can consider recorded seismic data to be the results of forward modeling experiments through subsurface structures. To image the reflectivity of the subsurface, we need to reverse the forward wave-propagation effects with an inverse of the forward modeling operator. Reverse time migration (RTM), the state-of-the-art imaging technology for complex structures (Baysal et al., 1983; Etgen et al., 2009; Zhang and Zhang, 2009), uses an adjoint modeling operator to approximate the inverse of the forward modeling. However, the accuracy of this approximation is degraded by spatial aliasing, limited aperture, noise, and non-uniform illumination due to complex overburden (Claerbout, 1992). As a result, the RTM image may have migration artifacts with limited bandwidth and uneven amplitudes (Gray, 1997).

Least-squares migration (LSM) was proposed to approximate the inverse of the forward modeling operator through either an iterative inversion (Tarantola, 1987; Schuster, 1993; Nemeth et al., 1999) or a single-iteration inversion (Hu et al., 2001; Rickett, 2003; Guitton, 2004; Lecomte, 2008). In recent years, least-squares reverse time migration (LSRTM) has attracted considerable attention (Wong et al., 2011; Dai et al., 2013; Zhang et al., 2013; Zeng et al., 2014). Improved image quality (both continuity and resolution), reductions in migration artifacts and noise, and better amplitudes are often cited as benefits of LSRTM; it is considered the next promising technology for subsalt imaging in the Gulf of Mexico (GOM).

### Theory

In this section, we discuss the general theory of LSM that is applicable to commonly used migration methods, including RTM, in both data and image domains. We also compare how different LSM methods invert the Hessian matrix

(Table 1). In addition, we outline an image-domain single-iteration LSM implementation in the curvelet domain.

#### 1. Data-domain and image-domain iterative LSM

Data-domain LSM inverts for a reflectivity model,  $m$ , to fit the recorded data,  $d_0$  (Tarantola, 1987; Schuster, 1993; Nemeth et al., 1999),

$$f_d(m) = \frac{1}{2} \|d_0 - Lm\|^2, \quad (1)$$

where  $f_d$  is the cost function to be minimized and  $L$  is the linearized Born modeling operator. Similarly, image-domain LSM (Tang, 2008; Aoki and Schuster, 2009) inverts for a reflectivity model to fit the raw migrated image,  $m_0 = L^T d_0$ ,

$$f_i(m) = \frac{1}{2} \|m_0 - L^T Lm\|^2, \quad (2)$$

where  $L^T$  is the migration operator. If  $L^T L$  is invertible, the least-squares solution for both Equations 1 and 2 is unique and thus the same:

$$m = (L^T L)^{-1} L^T d_0, \quad (3)$$

where  $L^T L$  is the so-called Hessian matrix,  $H$ .

Unfortunately, the size of  $H$  is too large to be stored on disk or in memory for real problems, and, therefore, a direct inverse of  $H$  is impractical. In practice, regardless of the invertibility of  $H$ , both Equations 1 and 2 can be iteratively solved by either steepest descent or conjugate gradient method (Lambaré et al., 1992). The gradient for Equation 1 can be written as:

$$g_d = L^T (d_0 - Lm), \quad (4)$$

and the gradient for Equation 2 can be written as:

$$g_i = L^T L (m_0 - L^T Lm). \quad (5)$$

For one iteration of LSM, the computation of  $g_d$  in Equation 4 costs one Born modeling and one migration; the computation of  $g_i$  in Equation 5 doubles this cost because of the cascade of modeling and migration operators. If 10 iterations are needed for the convergence of the inversion, the cost of data-domain and image-domain iterative LSM is at a level of 20 and 40 migrations (part of the computation for Born modeling and the migration may be shared to save some costs), respectively. This can be computationally prohibitive for modern 3D marine streamer data that uses RTM extensively for model building and the moderate- to high-frequency final migration.

#### 2. Image-domain single-iteration LSM

The key step of LSM is computing the inverse of the Hessian matrix. As discussed above, direct (Equation 3) or iterative (Equations 4 and 5) inversion methods are either impractical or very expensive. The cost-reducing alternative is to approximate the Hessian matrix. Lecomte (2008) and Fletcher et al. (2016) proposed to obtain the Hessian matrix using point spread functions (PSFs). The PSF method computes the impulse response (Hessian) on a coarse grid (to reduce interference between PSFs) of scattered points. The Hessian for every image point is obtained by interpolating between computed PSFs, and is then deconvolved from the raw migration image.

## LSRTM for subsalt imaging

Domain	Hessian inversion or approximation method	Theory	# of iterations	# of migrations per iteration
Data domain	Iterative	Cost objective: $\frac{1}{2}\ d_0 - Lm\ ^2$ ; Gradient: $L^T(d_0 - Lm)$ Output image: $m = (L^T L)^{-1} L^T d_0$	>10	~2
	Curvelet-domain Hessian filter (CHF) (single iteration)	Migration/modeling: $d_1 = L L^T d_0$ Cost objective: $\ C(d_0) - sC(d_1)\ ^2 + \epsilon\ s\ ^2$ Output image: $m = L^T C^{-1}( s C(d_0))$	1	~2
Image domain	Iterative	Cost objective: $\frac{1}{2}\ m_0 - L^T L m\ ^2$ ; Gradient: $L^T L(m_0 - L^T L m)$ Output image: $m = (L^T L)^{-1} L^T d_0$	>10	~4
	PSF deconvolution (single iteration)	Modeling/migration: $m_1 = L^T L m'$ ( $m'$ : point diffractors model) Output image: $m = \frac{m_0 m_1}{m_1 m_1 + \epsilon}$	1	~2 or more
	Curvelet-domain Hessian filter (CHF) (single iteration)	Modeling/migration: $m_1 = L^T L m_0$ Cost objective: $\ C(m_0) - sC(m_1)\ ^2 + \epsilon\ s\ ^2$ Output image: $m = C^{-1}( s C(m_0))$	1	~2

**Table 1:** Comparison of different LSM methods:  $d_0$  is the recorded data;  $m_0$  is the raw migration image;  $L^T$  is the migration operator;  $L$  is the Born modeling operator;  $C$  is the curvelet transform operator;  $C^{-1}$  is the inverse curvelet transform operator.

Guitton (2004) proposed to use non-stationary matching filters to approximate the inverse of the Hessian matrix in one iteration. In Guitton's approach, Born modeling is first performed using the migration velocity and the raw migration image,  $m_0$ , to obtain synthetic data,  $d_1 = L m_0$ , which is then remigrated to obtain a new image:

$$m_1 = L^T L m_0. \quad (6)$$

Next, non-stationary matching filters,  $F$ , are found by minimizing the following cost function:

$$f(F) = \frac{1}{2}\|m_0 - F m_1\|^2. \quad (7)$$

After obtaining  $F$ , the image-domain single-iteration LSM image can be written as:

$$m = F m_0. \quad (8)$$

Guitton (2004) computes multi-coefficient matching filters in the spatial domain (Rickett et al., 2001). Alternatively, we extend the idea of a guided image filter proposed by He et al. (2013) to formulate a curvelet-domain Hessian filter (CHF) for the following two reasons:

1. Multi-coefficient matching filters in the spatial domain may introduce unwanted event shifting because the relative amplitudes of events in  $m_0$  and  $m_1$  are different and some events in  $m_0$  may not exist in  $m_1$  and vice versa. By contrast, a zero-phase matching filter is more straightforward in the curvelet domain.
2. Events with different dips may need to be matched differently. In particular, the matching for crossing events (e.g., sedimentary terminations against faults or salt flanks) is better suited in the curvelet domain than in the spatial domain.

The cost function of the image-domain CHF can be written as

$$f(s) = \|C(m_0) - sC(m_1)\|^2 + \epsilon\|s\|^2, \quad (9)$$

where  $C$  is the curvelet transform operator,  $s$  is the matching filter, and  $\epsilon$  is a weighting factor for Tikhonov regularization. The final output image is

$$m = C^{-1}(|s|C(m_0)), \quad (10)$$

where  $C^{-1}$  is the inverse curvelet transform operator and  $||$  is used to remove the phase. Data-domain single-iteration LSM can also be implemented using this CHF scheme (the

second row in Table 1) or the scheme proposed by Khalil et al. (personal communication, 2016). Hereafter, we refer to CHF as the image-domain implementation.

### Application to synthetic data

We compared PSF, CHF, and data-domain iterative LSRTM using the BP2004 synthetic data. The acoustic forward-modeled, surface multiple-free data were generated using the velocity model shown in Figure 1a, along with a density model (not shown here). For the migration and Born modeling, a slightly smoothed version of Figure 1a was used. Figure 1b shows the reflectivity model that served as the ground truth for all three LSM methods.

In the raw RTM image ( $m_0$ ) migrated using the true velocity model (Figure 1c), we observed that, compared to the reflectivity in Figure 1b, the amplitude of subsalt events in Figure 1c was relatively weak due to poor illumination caused by the overburden salt. Figures 1d and 1e show the image after approximating the inverse of the Hessian using PSFs and CHF, respectively. Figure 1f shows the imaging results after 25 iterations of data-domain iterative LSRTM.

From this and other subsalt synthetic LSRTM tests, we concluded the following:

1. All three LSRTM methods - PSF, CHF, and iterative inversion - produced similar images with subsalt amplitude decay curves (Figure 1g) that matched the decay curve of the reflectivity model (the ground truth). However, none of these methods could recover the completely unimaged events (or those with extremely low amplitudes) in the raw RTM image.
2. Iterative inversion produced results comparable to those from the two single-iteration methods after ~20 iterations. This is consistent with Guitton's (2004) conclusion that a single-iteration LSRTM is a cost-effective alternative to iterative inversion.
3. As proposed by Fletcher et al. (2016), we computed interleaving grids to ensure sufficient isolation of PSFs before interpolation and used salt damping to minimize deconvolution instability around salt bodies. In addition,

we found a sparse deconvolution can be used to control noise (Sacchi, 1997).

4. In terms of computational efficiency and minimal manual controls, CHF appeared to be the most practical method for these tests.

We note that this test is not realistic because we did not include noise in the synthetic data, and we used the correct velocity model. The reality and possibilities for LSRTM for subsalt imaging would be better examined using field data in a more realistic context, i.e., with an inevitably inaccurate velocity model and residual noise.

### GOM field data example

A wide-azimuth streamer data set from Keathley Canyon, GOM was selected for the field data test. Although known for the well-defined salt geometries and overall good images, subsalt images in the area still suffer from uneven illumination, visible migration artifacts, and sub-optimal resolution. The input data underwent typical preprocessing to remove noise, ghost energy, multiples, etc. For this test we only compared results from CHF and data-domain iterative LSRTM.

When compared to the raw RTM image ( $m_0$ ) (Figure 2a), the CHF image (Figure 2b) had more balanced amplitude, less noise, and more continuous subsalt events, particularly those within the orange oval in Figure 2a. However, CHF did not appreciably increase vertical or lateral resolution, which was expected because (1) our input data were after source and receiver deghosting (i.e., the raw RTM image was broadband); (2) we generated  $m_1$  using a spiky source wavelet for the Born modeling and subsequent migration (narrowband source wavelet can be used to increase apparent resolution but may boost noise as well); and (3) no absorption was considered during the wave propagation.

Up to this point, we showed results of stack-based CHF described in Equations 9 and 10. Next, we extended the stack-based CHF to surface-offset gathers (SOGs) (Giboli et al., 2012):

$$f(s^{sog}) = \|C(m_0) - s^{sog}C(m_1^{sog})\|^2 + \epsilon\|s^{sog}\|^2, \quad (11)$$

$$m^{sog} = C^{-1}\left(|s^{sog}|C(m_0^{sog})\right). \quad (12)$$

Here the raw stacked image ( $m_0$ ) is used to design the guided filter for each offset class. We note that the zero-phased filter is important to retain event curvatures.

Figure 2e shows three raw RTM SOGs ( $m_0^{sog}$ ) spanning the stacked image in Figure 2a, while Figure 2f shows the same gathers after CHF ( $m^{sog}$ ). We observed that SOGs after CHF had a higher signal-to-noise ratio and more continuous subsalt events across all offsets and still retained the event curvatures. In practice, CHF SOGs can be used to improve the difficult task of subsalt tomographic velocity updating. A stacked image from SOG-based CHF (Figure 2c) showed further reduction of noise when compared with the stacked image from stack-based CHF (Figure 2b).

Similar to single-iteration CHF results, data-domain iterative LSRTM produced more balanced amplitude in the

subsalt region. After 10 iterations, the resolution of the subsalt region was visibly higher than the raw stack and the two CHF stacks (Figure 2d). However, the noise content also increased. The increased noise was mostly from a wider bandwidth as well as multiple scattering energy due to the presence of the salt body (and other strong contrasts) in the velocity model used for Born modeling and the subsequent migration.

The quality of subsalt images can be judged by noise, event coherency, amplitude consistency, and resolution. Within the prospective Lower Tertiary interval (denoted by up-down arrows in Figure 2) in the region, single-iteration CHF performed better in terms of noise suppression, while the iterative method yielded higher resolution but also produced strong noise from the multiple scattering. All methods were effective at removing uneven amplitudes for this test area.

### Discussion

Using BP2004 synthetic and GOM field data, we demonstrated that both image-domain single-iteration and data-domain iterative LSRTM methods can reduce uneven subsalt amplitudes.

The PSF method computes the exact impulse response (Hessian) at each scattered point. It is theoretically precise for image points where PSFs are computed. However, PSFs computed on a sparse grid (to reduce interference) need to be interpolated to each imaging point and then deconvolved from the raw image point-by-point. The interpolation of PSFs and point-by-point deconvolution are challenging in practice and may sometimes cause inaccuracy and instability for areas with complex structures.

Instead of deconvolving PSFs, matching-filter methods such as CHF deconvolve a demigrated/remigrated image ( $m_1$ ) from the original image ( $m_0$ ). The image used for the deconvolution is the weighted-stack of impulse responses for all the image points within a given spatial window. This means that CHF is inherently more stable than the PSF method, although it may not be able to fully compensate for unbalanced amplitude and limited bandwidth. In addition, as a guided filter in the curvelet domain, the CHF can effectively attenuate migration artifacts and other noise without smearing the image, like many post-migration denoise processes.

In both the PSF and CHF cases, the 3D spatial window needs to be large enough for a stable deconvolution. On the other hand, the deconvolution is preferably performed in a relatively small spatial window to better honor any local variations of the Hessian matrix. This means that migration artifacts and illumination patterns on the large scale may not be well handled by those two approaches. Iterative LSRTM based on full-window global minimization does not have this limitation.

In practice, iterative LSRTM has not been widely used for subsalt imaging primarily because iterative LSRTM is computationally expensive due to its slow convergence rate (if converges at all) that stems from large discrepancies

## LSRTM for subsalt imaging

between the recorded data and acoustic Born-modeled data. Furthermore, a more theoretically accurate approximation of the inverse of the Hessian, iterative LSRTM, is inherently more sensitive to noise, internal multiples, velocity errors, and the source wavelet. Further research on iterative inversion methods is still required for iterative LSRTM methods to produce superior subsalt results over single-iteration methods.

### Conclusions

The raw RTM subsalt image obtained from the input data and the migration velocity model largely limits the performance of all the LSRTM methods. It is very difficult, if not impossible, to use any LSRTM methods to recover events that are completely unimaged due to very poor illumination and/or an inaccurate velocity model. A better input seismic data set can enhance the images in two ways: by providing additional subsurface information for imaging and by increasing our ability to derive a higher quality velocity model. A case in point is the advancement of full-azimuth acquisition in the GOM, which not only leads to better subsalt images, but also produces higher fidelity

velocity models than would be obtained from a wide-azimuth data set.

As counterintuitive as it seems, we may be able to use LSRTM to improve the velocity model, even though it assumes the velocity model is correct. One possibility might be to interleave LSRTM with key velocity model building steps, e.g. using the SOGs generated from CHF for better curvature picking and, in turn, better tomographic inversion. Of course, the computation of interleaving LSRTM with velocity estimation can be costly.

LSRTM has shown promising impact on subsalt imaging. Through additional synthetic and field data tests, the subsalt imaging community can continue to improve the algorithms and bring LSRTM closer to its full potential.

### Acknowledgements

We thank BP for the 2004 2D model and CGG for permission to present this work. We also thank Shouting Huang for preparing the field data examples. We are grateful to Adel Khalil for his research that has inspired us.

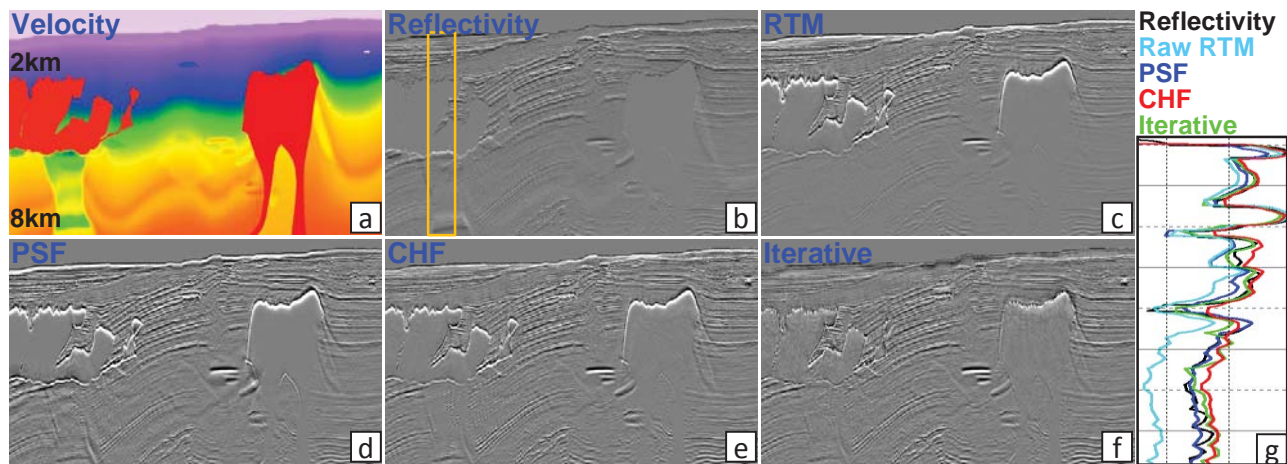


**Figure 1:** BP2004 synthetic study: (a) velocity model used for modeling and migration; (b) reflectivity model derived from density and velocity model and used as the ground truth; (c) RTM image using forward modeling synthetic data; (d) image after PSF deconvolution; (e) image after CHF; (f) data-domain iterative LSRTM image; (g) amplitude decay curves (orange box in b) for images in b-f.

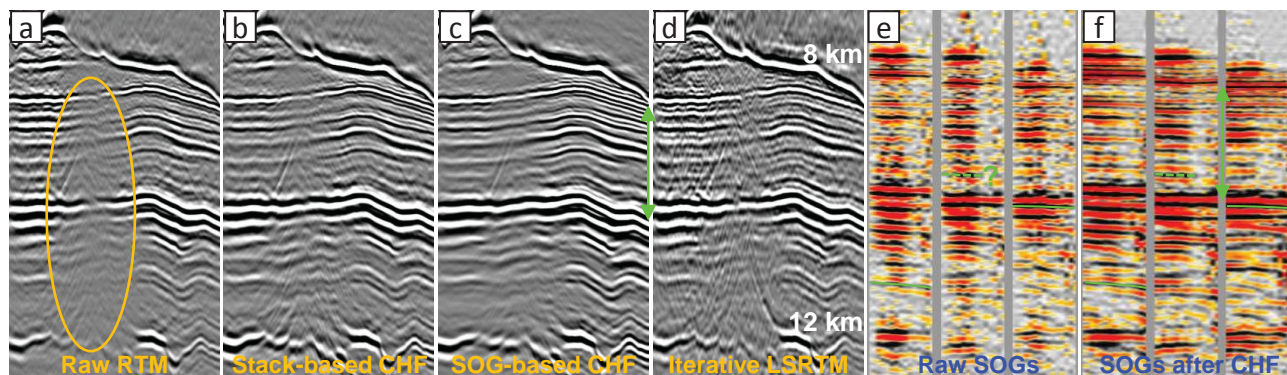


**Figure 2:** GOM field data example: Stacked images-(a) raw RTM using input data after shot and receiver deghosting; (b) image after stack-based CHF; (c) image after SOG-based CHF; (d) image after data-domain iterative LSRTM; and SOGs-(e) raw SOGs; and (f) SOGs after CHF. Gather curvatures marked by solid green lines remain unchanged before (e) and after (f) CHF. Dashed green lines indicate a curvature that can be easily picked using SOGs after CHF. The prospective Lower Tertiary interval is indicated by green up-down arrows on Figures 2c and 2f.

## EDITED REFERENCES

Note: This reference list is a copyedited version of the reference list submitted by the author. Reference lists for the 2016 SEG Technical Program Expanded Abstracts have been copyedited so that references provided with the online metadata for each paper will achieve a high degree of linking to cited sources that appear on the Web.

## REFERENCES

- Aoki, N., and G. Schuster, 2009, Fast least-squares migration with a deblurring filter: *Geophysics*, **74**, no. 6, WCA83–WCA93, <http://dx.doi.org/10.1190/1.3155162>.
- Baysal, E., D. Kosloff, and J. Sherwood, 1983, Reverse-time migration: *Geophysics*, **48**, 1514–1524, <http://dx.doi.org/10.1190/1.1441434>.
- Claerbout, J. F., 1992, *Earth soundings analysis: Processing versus inversion*: Blackwell Scientific Publications.
- Dai, W., Y. Huang, and G. T. Schuster, 2013, Least-squares reverse time migration of marine data with frequency-selection encoding: *Geophysics*, **78**, no. 4, S233–S242, <http://dx.doi.org/10.1190/geo2013-0003.1>.
- Etgen, J., S. Gray, and Y. Zhang, 2009, An overview of depth imaging in exploration geophysics: *Geophysics*, **74**, no. 6, WCA5–WCA17, <http://dx.doi.org/10.1190/1.3223188>.
- Fletcher, R. P., D. Nichols, R. Bloor, and R. T. Coates, 2016, Least-squares migration — Data domain versus image domain using point spread functions: *The Leading Edge*, **35**, 157–162, <http://dx.doi.org/10.1190/tle35020157.1>.
- Giboli, M., R. Baina, L. Nicoletis, and B. Duquet, 2012, Reverse time migration surface offset gathers, part 1: A new method to produce 'classical' common image gathers: 82nd Annual International Meeting, SEG, Expanded Abstracts, 1–5, <http://dx.doi.org/10.1190/segam2012-1007.1>.
- Gray, S. H., 1997, True-amplitude seismic migration: A comparison of three approaches: *Geophysics*, **62**, 929–936, <http://dx.doi.org/10.1190/1.1444200>.
- Guitton, A., 2004, Amplitude and kinematic corrections of migrated images for nonunitary imaging operators: *Geophysics*, **69**, 1017–1024, <http://dx.doi.org/10.1190/1.1778244>.
- He, K., J. Sun, and X. Tang, 2013, Guided image filtering: *IEEE Transactions on Pattern Analysis and Machine Intelligence*, **35**, 1397–1409, <http://doi.ieeecomputersociety.org/10.1109/TPAMI.2012.213>, <http://dx.doi.org/10.1109/TPAMI.2012.213>.
- Hu, J., G. T. Schuster, and P. A. Valasek, 2001, Poststack migration deconvolution: *Geophysics*, **66**, 939–952, <http://dx.doi.org/10.1190/1.1444984>.
- Lambaré, G., J. Virieux, R. Madariaga, and S. Jin, 1992, Iterative asymptotic inversion in the acoustic approximation: *Geophysics*, **57**, 1138–1154, <http://dx.doi.org/10.1190/1.1443328>.
- Lecomte, I., 2008, Resolution and illumination analyses in PSDM: A ray-based approach: *The Leading Edge*, **27**, 650–663, <http://dx.doi.org/10.1190/1.2919584>.
- Nemeth, T., C. Wu, and G. T. Schuster, 1999, Least-squares migration of incomplete reflection data: *Geophysics*, **64**, 208–221, <http://dx.doi.org/10.1190/1.1444517>.
- Rickett, J. E., 2003, Illumination-based normalization for wave equation depth migration: *Geophysics*, **68**, 1371–1379, <http://dx.doi.org/10.1190/1.1598130>.
- Rickett, J. E., A. Guitton, and D. Gratwick, 2001, Adaptive multiple subtraction with non-stationary helical shaping filters: 63rd Annual Meeting, EAGE, Extended Abstracts, P167.
- Sacchi, M. D., 1997, Reweighting strategies in seismic deconvolution: *Geophysical Journal International*, **129**, 651–656, <http://dx.doi.org/10.1111/j.1365-246X.1997.tb04500.x>.
- Schuster, G. T., 1993, Least-squares crosswell migration: 63rd Annual International Meeting, SEG, Expanded Abstracts, 110–113, <http://dx.doi.org/10.1190/segam2012-1425.1>.

- Tang, Y., 2008, Wave-equation Hessian by phase encoding: 78th Annual International Meeting, SEG, Expanded Abstracts, 2201–2205, <http://dx.doi.org/10.1190/1.3059323>.
- Tarantola, A., 1987, Inverse problem theory: Methods for data fitting and model parameter estimation: Elsevier Science Publishing Company.
- Wong, M., S. Ronen, and B. Biondi, 2011, Least-squares reverse-time migration/inversion for ocean bottom data: A case study: 81st Annual International Meeting, SEG, Expanded Abstracts, 2369–2373, <http://dx.doi.org/10.1190/1.3627684>.
- Zeng, C., S. Dong, and B. Wang, 2014, Least-squares reverse time migration: Inversion-based imaging toward true reflectivity: The Leading Edge, **33**, 962–968, <http://dx.doi.org/10.1190/tle33090962.1>.
- Zhang, Y., L. Duan, and Y. Xie, 2013, A stable and practical implementation of least-squares reverse time migration: 83rd Annual International Meeting, SEG, Expanded Abstracts, 3716–3720, <http://dx.doi.org/10.1190/segam2013-0577.1>.
- Zhang, Y., and H. Zhang, 2009, A stable TTI reverse time migration and its implementation: 79th Annual International Meeting, SEG, Extended Abstracts, 2794–2798, <http://dx.doi.org/10.1190/1.3255429>.